Journal of
Sensor and
Actuator Networks

Article

Electrostatic MEMS Phase Shifter for SiN Photonic Integrated Circuits

Seyedfakhreddin Nabavi *, Michaël Ménard and Frederic Nabki

Department of Electrical Engineering, École de Technologie Supérieure, Montreal, QC H3C 1K3, Canada; michael.menard@etsmtl.ca (M.M.); frederic.nabki@etsmtl.ca (F.N.)
* Correspondence: snabavi@mun.ca

Abstract

Optical phase modulation is essential for a wide range of silicon photonic integrated circuits used in communication applications. In this study, an optical phase shifter utilizing photo-elastic effects is proposed, where mechanical stress is induced by electrostatic micro-electro-mechanical systems (MEMS) with actuators arranged in a comb drive configuration. The design incorporates suspended serpentine silicon nitride (SiN) optical waveguides. Through extensive numerical simulations, it is shown that the change in the effective refractive index (n_{eff}) of the optical waveguide is a function of the voltage applied to the electrostatic actuators and that such n_{eff} tuning can be achieved for a broad range of wavelengths. Implemented within one arm of an unbalanced Mach–Zehnder interferometer (MZI), the phase shifter achieves a phase change of π when the stressed optical path measures 4.7 mm, and the actuators are supplied with 80 V DC and consume almost no power. This results in a half-wave voltage-length product ($V_{\pi}L$) of 37.6 V·cm. Comparative analysis with contemporary optical phase shifters highlights the proposed design's superior power efficiency, compact footprint, and simplified fabrication process, making it a highly efficient component for reconfigurable MEMS-based silicon nitride photonic integrated circuits.

Keywords: MEMS; optical; silicon photonic; electrostatics

Academic Editor: Adnan M. Abu-Mahfouz

Received: 3 June 2025
Revised: 15 August 2025
Accepted: 22 August 2025
Published: 29 August 2025

Citation: Nabavi, S.; Ménard, M.; Nabki, F. Electrostatic MEMS Phase Shifter for SiN Photonic Integrated Circuits. *J. Sens. Actuator Netw.* **2025**, *14*, 88. https://doi.org/10.3390/jsan14050088

Correction Statement: This article has been republished with a minor change. The change does not affect the scientific content of the article and further details are available within the backmatter of the website version of this article.

1. Introduction

Recent advancements in data density within communication networks have exposed significant limitations in traditional copper-based interconnects, such as loss, dispersion, crosstalk, and speed constraints. Silicon photonics has emerged as a leading solution to these challenges, offering the potential for low cost and enhanced performance through photonic and electronic integration, and compatibility with complementary metal–oxide semiconductor (CMOS) electronics manufacturing technologies [1].

Modulating optical signals is a crucial functionality in photonic circuits. An optical modulator alters various beam parameters such as amplitude, polarization, or phase as light propagates [2]. This can be applied to optical sensing platforms, such as optical gyroscopes, where phase modulation may contribute to the suppression of noise [3]. Optical phase modulation can be classified into permanent and tunable techniques. Permanent phase modulation involves a fixed adjustment of the phase of the optical signal, typically achieved through unbalanced optical path length or material changes. Conversely, tunable phase modulation allows dynamic, adjustable changes, providing control over the optical signal phase as needed.

The alteration of the effective refractive index (n_{eff}) is central to the phase modulation process. As shown in Figure 1, configurable optical phase shifters can be implemented using four primary methods: thermo-optic, electro-optic, physical movement, and photo-elastic effects. Each method has distinct advantages and limitations, assessed through performance metrics such as modulation speed, optical bandwidth, insertion loss, footprint, efficiency, and power consumption.

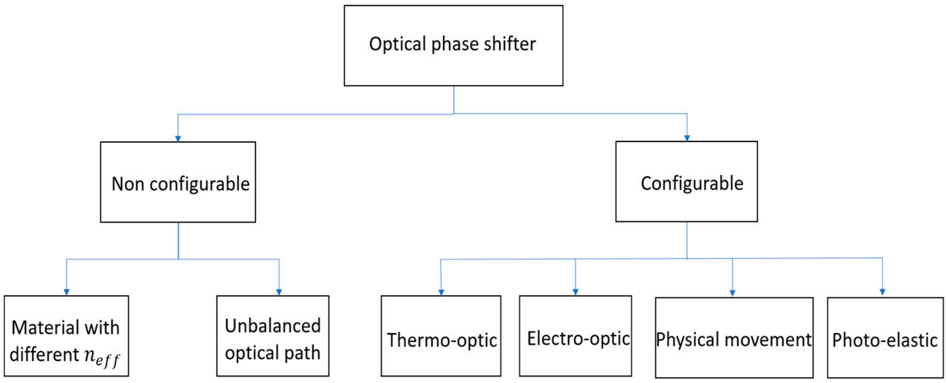

Figure 1. Classification of optical phase shifters: non-configurable vs. configurable. Configurability is preferred so that a single device can have multiple functions.

Thermo-optic phase shifters use thermal energy to alter n_{eff} by positioning thermal electrodes near or over optical waveguides. For example, Sun et al. [4] designed and demonstrated a polarization-insensitive 4 × 4 optical matrix switch, in which 2 × 2 Mach–Zehnder interferometers integrated with a pair of resistive metal heaters are used to modulate the phase. Although the thermo-optic mechanism allows dynamic modulation, it is relatively slow and requires high electrical power [5]. The heat generated can also affect adjacent components in compact systems.

In contrast, electro-optic modulators offer high-speed, power-efficient phase modulation by placing optical waveguides between electrodes and applying an external voltage to create an electric field, changing n_{eff} through the Pockels effect [6]. However, this method is limited to non-centrosymmetric materials such as lithium niobate ($LiNbO_3$), which are often incompatible with CMOS technologies [7,8]. Although aluminum nitride (AlN) is proposed to achieve CMOS compatibility, its significantly lower Pockels coefficient (i.e., 33 times lower) compared to $LiNbO_3$ results in inefficient phase modulation [9,10].

Physical-movement-based phase shifters employ micro-electro-mechanical systems (MEMS) technology to physically displace optical waveguides integrated into a movable mechanical structure. Typically, these systems comprise fixed and movable waveguides. By applying electrostatic forces, the movable waveguide can be brought closer to the fixed waveguide, interacting with the evanescent field and resulting in a phase shift. For instance, Edinger et al. [11] demonstrated an optical phase shifter that enables a phase shift of 2.9 π when the air gap between the moving and fixed waveguides is adjusted from 175 nm to 500 nm using an actuation voltage of 36 V. This approach necessitates advanced microfabrication techniques and sophisticated mechanical designs, as the air gap between the waveguides must be maintained at the nanometer scale. Achieving such precise control over the air gap and ensuring reliable actuation requires meticulous engineering and fabrication processes, making it a challenging yet effective method for optical phase modulation. On the other hand, MEMS-based devices often require high actuation voltages to achieve effective modulation [12], and repeated mechanical movements can lead to system fatigue over time, which can affect the overall lifetime of the device [13].

Alternatively, photo-elastic optical phase shifters modulate the optical phase by applying mechanical stress to the waveguides, resulting in changes to n_{eff}. Previous implementations have utilized piezoelectric actuators to apply this stress. For instance, Sebbag et al. [14] demonstrated an optical phase shifter where an electrically controlled piezoelectric actuator, made of lead zirconate titanate (PZT), applies stress to the waveguide. By increasing the applied voltage, a change in n_{eff} of 1.8×10^{-4} was achieved, and this change was reversible in the absence of an external voltage. Similarly, Wang et al. [15] proposed a micro-resonator modulator using a piezoelectric actuator on top of a silicon nitride (SiN) waveguide to induce mechanical stress, altering n_{eff}. Although these methods offer significant advantages, such as effective phase modulation, they introduce added complexity in the manufacturing process due to the need for additional deposition steps for piezoelectric materials and their electrodes. This increased fabrication complexity can be a limiting factor, particularly in applications where simplicity and reduced manufacturing steps are paramount.

This study proposes a configurable optical phase shifter based on photo-elastic effects, leveraging the advantages of electrostatic MEMS actuators. Unlike previous implementations that relied on piezoelectric materials, this design employs electrostatic actuators positioned near the waveguide to induce mechanical stress. The use of electrostatic actuation offers several benefits, including a fast response time, low power consumption, and a reduced number of microfabrication steps compared to piezoelectric-based methods. The proposed phase shifter is implemented within one arm of an unbalanced Mach–Zehnder interferometer (MZI). The design features a suspended serpentine SiN optical waveguide integrated with electrostatic actuators arranged in a comb-drive configuration. It is worth pointing out that SiN-based optical waveguides offer several distinct advantages, including low propagation losses, a broad operating range from the visible to near-infrared spectrum, reduced sensitivity to temperature variations, and high power handling capacity [16,17]. Furthermore, these waveguides are compatible with CMOS fabrication technology [18], making them well-suited for large-scale photonic integration.

In the proposed phase shifter, by applying a DC voltage to its actuators, the waveguide is subjected to mechanical stress, resulting in changes to n_{eff} and enabling dynamic phase modulation. Numerical simulations show that a phase change of π can be achieved when the optical path under stress measures 4.7 mm, and the actuators are supplied with 80 V DC, consuming virtually no power. This results in a half-wave voltage-length product ($V_{\pi}L$) of 37.6 V·cm, indicating a highly efficient phase modulation. Hence, the contributions of the present study can be summarized as follows:

1. A novel electrostatic MEMS phase shifter operating based on the photo-elastic effect is proposed.
2. The proposed design leverages the unique advantages of electrostatic actuation, such as near-zero power consumption and a simplified fabrication process.
3. The structure of the phase shifter is devised to accommodate the optical SiN waveguide within its moving parts, ensuring compatibility with integrated photonics platforms.
4. The applicability of the proposed phase shifter is demonstrated through its ability to induce a sufficient phase shift to generate deep intensity when implemented in one arm of an MZI.

2. Relevance to Sensor and Actuator Networks

With the rapid advancement of MEMS and microelectronic technologies, Wireless Sensor Networks (WSNs) and the Internet of Things (IoT) have become predominant solutions for enabling distributed devices to sense, communicate, share data, and be remotely monitored or controlled [19]. In such networks, photonic devices play a key role in enabling high-bandwidth, low-latency communication and precise sensing [20]. The proposed electrostatic MEMS phase shifter offers unique characteristics, low power consumption, batch fabrication, and potential for large-scale integration, which make it particularly suitable for deployment in sensor and actuator networks. Hence, the device can serve as a reconfigurable optical element within these nodes, providing effective and efficient phase control for wavelength routing, interferometric sensing, and noise suppression.

3. Theory

A schematic representation of a typical optical waveguide is shown in Figure 2. As shown in this figure, the optical waveguide has a core surrounded by a cladding layer. The specific distribution of the refractive index for such an optical waveguide depends on the geometry and material properties of the waveguide and varies along the x-axis and y-axis. In this context, the refractive index changes abruptly at the interface layers and can be defined by a step function as follows:

$$n(x,y) = \begin{cases} n_{core}, \; if \; 0 < x < w \; and \; 0 < y \leq h \\ n_{clad}, \; \; otherwise \end{cases} \tag{1}$$

where n_{core} is the refractive index of the waveguide core, n_{clad} is the refractive index of the waveguide cladding, w is the width of the waveguide core, and h is the height of the waveguide core.

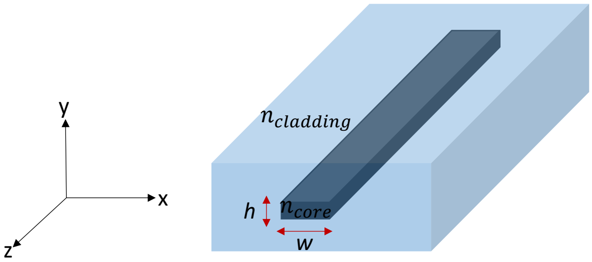

Figure 2. Schematic representation of the optical waveguide, showing the positioning of the core and cladding layers.

The optical phase shift produced by alterations of the effective index includes changes in both the refractive indices of the core and cladding layers, and it can be estimated as follows:

$$\Delta\phi = \frac{2\pi}{\lambda} L \, \Delta n_{eff} \tag{2}$$

where ϕ is the optical phase, λ is the wavelength of the propagating wave, L is the optical path, and Δn_{eff} represents changes in the effective refractive index.

n_{eff} is a function of the propagation constant, β, and can be calculated as given below:

$$n_{eff} = \frac{\beta}{k} \tag{3}$$

where k is the wavenumber, which is equal to $2\pi/\lambda$.

On the other hand, the electric field propagation along the z-axis in the context of time-harmonic fields can be expressed as follows [21]:

$$E = E(x,y)e^{j(\omega t - \beta z)} = \left(E_x(x,y) + E_y(x,y) + E_z(x,y)\right)e^{j\left(\frac{2\pi}{\lambda}t - \beta z\right)} \tag{4}$$

where $E_{x,y,z}$ (x,y) are components of the electric field vector in the xy-plane, and t is the time constant. Therefore, the components of the electric field in the waveguide determine the propagation constant and eventually n_{eff}.

According to photo-elastic effects, the changes in the refractive index of the material caused by mechanical stress can be expressed as follows [22]:

$$n_x = n_0 - \left(C_1\sigma_x + C_2\left(\sigma_y + \sigma_z\right)\right),\\ n_y = n_0 - \left(C_1\sigma_y + C_2(\sigma_x + \sigma_z)\right) \tag{5}$$

where n_x and n_y are the refractive index components of the material obtained under the applied mechanical stress, n_0 is the bulk refractive index in the absence of stress, σ_x, σ_y, and σ_z are the relative stress components, and C_1 and C_2 are the stress-optic (i.e., photo-elastic) coefficients related to the Young's modulus, Poisson's ratio, and photo-elastic tensor elements of the material.

Mechanical stress results from the application of force over a specific area. In this study, the mechanical force is generated by a series of electrostatic actuators. A comb drive structure, configured with parallel plate electrodes, converts the excitation voltage into a mechanical force, as illustrated in Figure 3. In this configuration, the comb drive comprises a series of fixed and movable fingers. When a DC voltage is applied, electrostatic attraction forces develop between the fingers, causing the movable structure to shift in the direction of the generated electrostatic force. This movement induces the required mechanical stress in the optical waveguide, enabling effective phase modulation through the photo-elastic effect.

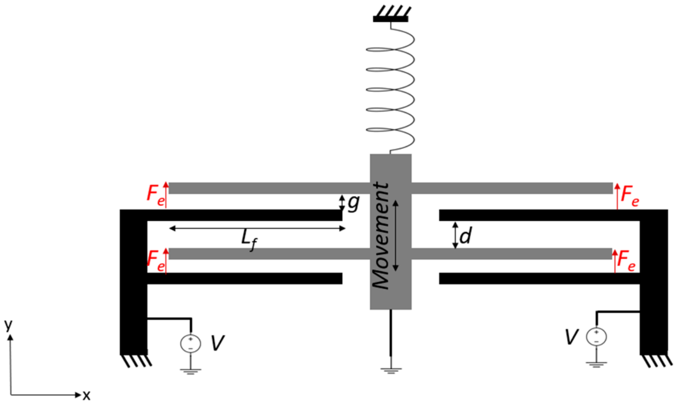

Figure 3. Schematic diagram of the electrostatic actuator using a series of fingers in the form of a parallel plate.

The capacitance between two parallel plates can be estimated as follows:

$$C = \frac{\varepsilon_0 \times L_f \times t}{g} \tag{6}$$

where ε_0 is the permittivity constant of free space, L_f is the overlap length between the fixed and movable electrodes, t is the thickness of the fingers, and g is the distance between two fingers. Since $g << d$, the capacitance between the fingers has a smaller value with the air gap size of g, such that the electrostatic force generated with the air gap size of d, although it has an opposite direction, is negligible. Consequently, the effective direction of the generated electrostatic force, F_e is upward along the y-axis, as labeled in Figure 3.

The electrostatic force acting on the surface of fingers is given by the following [23]:

$$F_e = \frac{\partial U}{\partial y} = \frac{1}{2}\frac{\partial c}{\partial y}V^2 = \frac{\varepsilon_0 \times L_f \times t \times N}{g}V^2 \tag{7}$$

where U is the energy associated with the applied electrical voltage V, y is the displacement in the y-direction, and N is the number of finger pairs on both sides of the actuator.

The consideration of (1), (5), and (7) indicates that the refractive indices of both the cladding and core of the waveguide can be altered by the driving voltage of the electrostatic actuator when the actuator interacts with the optical waveguide. This interaction induces mechanical stress, resulting in a change in n_{eff} and consequently causing a phase shift, $\Delta\phi$.

4. Design and Modeling

Figure 4 presents a structural diagram of the electrostatic MEMS optical phase shifter, which comprises a serpentine suspended beam supporting the optical waveguide above it. Two distinct groups of electrostatic actuators are positioned along the upper and lower parts of the optical path. One group features a larger air gap, while the other has a smaller air gap. The use of different actuators addresses the varying stiffness of the structure, particularly at points far from the anchoring points, where the optical path bends at 180 degrees. Actuators with a larger air gap are strategically placed in these areas to prevent contact between the fixed and moving fingers during large motions when all actuators are activated. Additionally, this configuration allows all six actuators to operate with an identical excitation voltage, simplifying the driving circuitry.

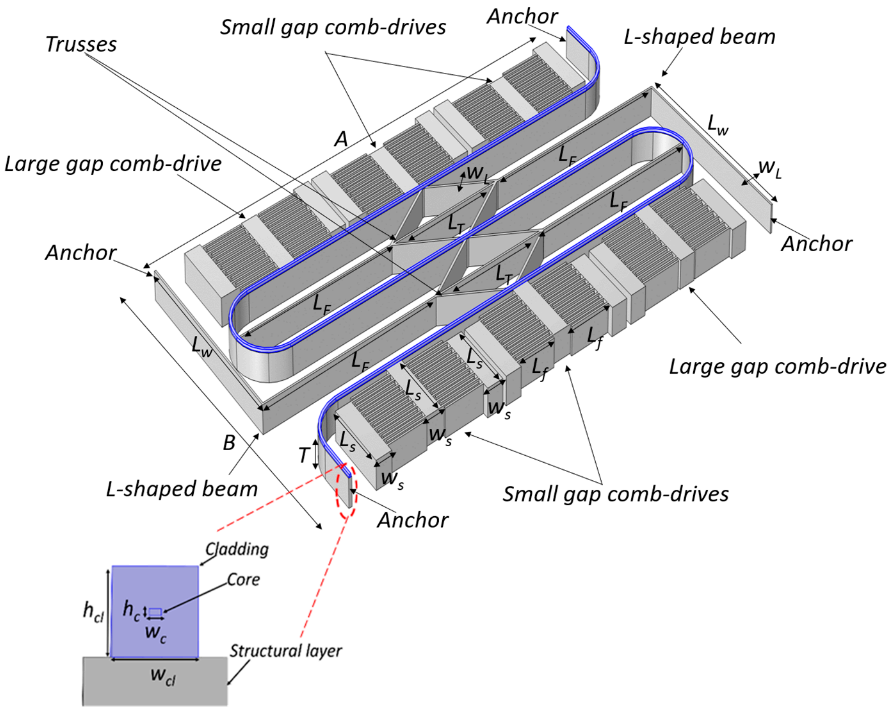

Figure 4. Structural diagram of the electrostatic MEMS optical phase shifter.

To enhance the durability of the suspended structure, two mechanical trusses are integrated into the center of the device. One side of each truss is affixed to the curved segment of the serpentine beam, while the other side is anchored through an L-shaped beam. Each L-shaped beam is fixed on the opposite side at a certain distance from the anchoring point of the suspended serpentine beam. The serpentine beam is bent at an angle of 110 degrees to minimize optical loss. Consequently, the proposed MEMS electrostatic optical phase shifter features a symmetric geometry, allowing the optical signal to enter from one side and exit from the other. In this mechanical design, the activation of each actuator induces stress in the optical waveguide, facilitating phase modulation.

The MEMS structural layer in this study consists of a thick silicon (Si) layer. It supports an optical waveguide with a SiN core surrounded by a silicon dioxide (SiO_2) cladding. Figure 5 presents a cross-sectional view of the optical waveguide integrated onto the suspended structure. This suspended structure can be deformed by applying a mechanical force. The manufacturability and applicability of such a suspended mechanical structure with integrated optical waveguides have been successfully demonstrated in our prior work for creating optical switches [24,25] and aligners [26,27]. While the specific phase shifter proposed in this study has not yet been fabricated, its core components, namely, the suspended SiN waveguide and comb drive electrostatic actuators, are consistent with those used in our previously demonstrated devices. These components have been shown to be reliably fabricated with high yield and reproducibility [28]. The physical dimensions of the electrostatic MEMS optical phase shifter are listed in Table 1.

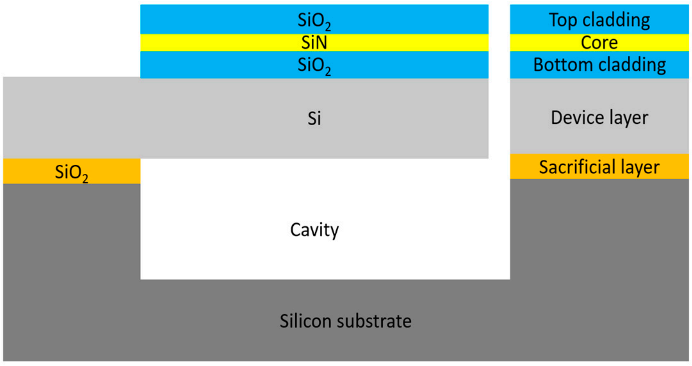

Figure 5. Cross-sectional view of the suspended structure of the electrostatic MEMS optical phase shifter illustrating the configuration of the mechanical and optical layers. The process flow complies with the manufacturing process of AEPONYX Inc., Montreal, Quebec, Canada [29].

Table 1. Physical dimensions of the electrostatic MEMS optical phase shifter.

Parameters	Description	Value (μm)
A	Overall chip length	1400
B	Overall chip width	850
L_w	Web length of the L-shaped beam	527
L_F	Flange length of the L-shaped beam	557
L_T	Length of the mechanical truss	350
L_s	Length of the comb drive support	180
w_s	Width of the comb drive support	50
L_f	Overlap comb drive fingers	120
g_s	Gap size of the small-gap comb drive	4
g_L	Gap size of the large-gap comb drive	6
ds	Finger spacing of the small-gap comb drive	6
d_L	Finger spacing of the small gap comb drive	8
w_L	Width of the L-shaped beam and truss	5
w_a	Width of the serpentine beam	10
h_c	Height of the waveguide core	0.450
w_c	Width of the waveguide core	0.850
h_{cl}	Height of the waveguide cladding	6.4
w_{cl}	Width of the waveguide cladding	6
T	Thickness of the structural layer	59

5. Results and Discussion

The suitability of the proposed technique for generating an optical phase shift via electrostatic force was comprehensively investigated through numerical simulations performed using COMSOL Multiphysics (version 6.1). Initially, the stress distribution in the optical waveguide was analyzed when the structural layer was subjected to an axial force with an amplitude of 5 mN. Figure 6 presents the stress profiles of the integrated optical waveguide under both compressive and tensile forces. The stress distribution in the structural layer was found to be nearly identical for both types of stress. However, under tensile stress, both the core and cladding of the optical waveguide experienced greater stress. This difference is primarily due to the physical properties of the structural layer, which, being relatively thick, absorbs a significant amount of stress. In the case of tensile forces, the stress propagates vertically through the y-axis, reaching the optical stack more effectively. It is worth mentioning that in the proposed optical phase shifter, mechanical stress cannot be directly applied to the optical stack due to the height difference between the actuators, formed by the structural layer, and the optical stack, which is constructed on the surface of the structural layer.

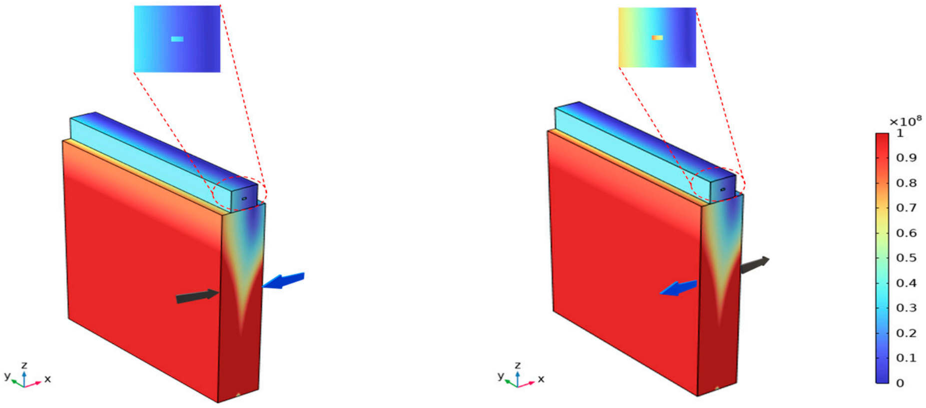

(**a**) (**b**)

Figure 6. Graphical representation of the stress profiles in the optical waveguide and structural layer when the structural layer is subjected to axial (**a**) compressive and (**b**) tensile forces. The black and blue arrows indicate the directions of the applied force and reaction force, respectively.

To quantitatively investigate the effects of the amplitude and type of applied force on the stress experienced by the optical stack, Figure 7 illustrates the average stresses as a function of varying compressive and tensile forces. For small applied forces (i.e., below 8 mN), the observed stress under both tensile and compressive forces is nearly equal. As the force amplitude increases, the optical stack experiences slightly greater stress from the tensile force. For instance, under a larger tensile force of 28 mN, the optical stack received an average von Mises stress of 3.8 MN/m^2, compared to 3.7 MN/m^2 under compressive force. This indicates that the optical stack is slightly more stressed under higher tensile forces.

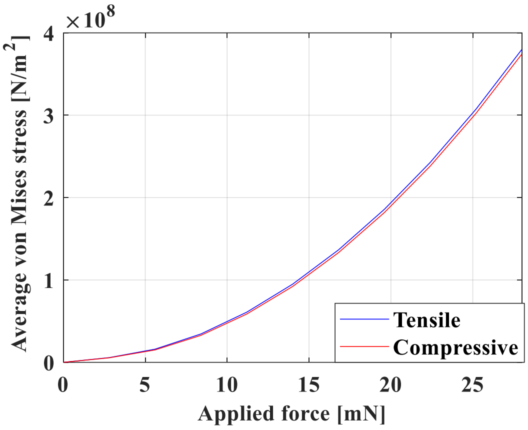

Figure 7. Average stress received by the optical stack as a function of applied force for compressive and tensile forces.

To further investigate the relationship between the stress applied to the optical stack and the changes in n_{eff}, simulations were conducted to compute the variations in n_{eff} as a function of the applied axial compressive and tensile forces. The results, shown in Figure 8, indicate a trend consistent with the predictions of the stress study, revealing a quadratic response where Δn_{eff} increases with the applied force. Comparing the effects of compressive and tensile forces, it was found that Δn_{eff} is greater by a magnitude of 3.5×10^{-5} under a sufficiently large tensile force. Although this difference may appear minimal, it is significant when integrated along the length of the optical path, where such a small deviation can result in a considerable phase shift under tensile forces compared to compressive forces.

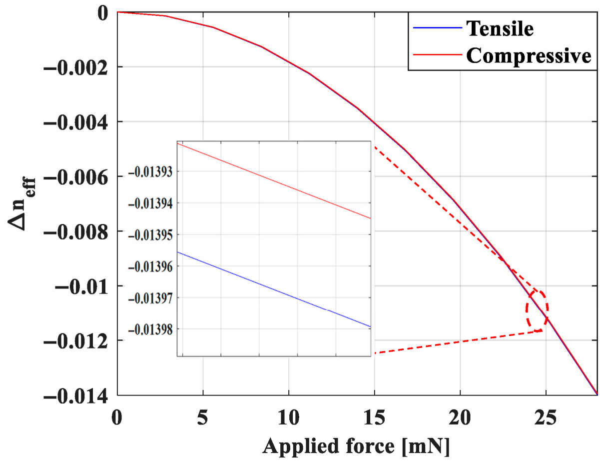

Figure 8. Effective index changes as a function of applied force for compressive and tensile forces.

It has been established that axially applied tensile forces can alter the n_{eff} of SiN waveguides. To illustrate that the electrostatic MEMS optical phase shifter presented above is an effective solution for applying tensile stress to an integrated optical waveguide, its mechanical behavior was analyzed. Initially, the device functionality was examined in the frequency domain. Figure 9 shows the simulated resonant modes and frequency spectra of the electrostatic optical MEMS phase shifter. The first three resonant modes occur at frequencies of 5.28 kHz, 8.4 kHz, and 13.02 kHz. At the fundamental resonant frequency (i.e., 5.28 kHz), the device exhibits the largest deflection along the y-axis. Similarly, at the third resonant frequency, significant in-plane movement is observed, with maximum deflections along both the y-axis and the x-axis. In contrast, at the second resonant frequency, the movement is predominantly out-of-plane, with the maximum deflection along the z-axis. These results indicate that the phase shifter has a lower stiffness coefficient along its in-plane axes (x- and y-axis) where the actuators are positioned. Consequently, when the actuators are activated, the device deforms primarily in-plane.

The effectiveness of the MEMS electrostatic optical phase shifter design in applying stress to the integrated optical waveguide when the actuators are activated was investigated through a static study. In this analysis, the electrostatic actuators were activated with a DC voltage of 120 V. Figure 10a illustrates graphically the deformation of the electrostatic MEMS optical phase shifter, magnified by a factor of 20. Figure 10b presents the deformation profile along the optical path length, revealing that the device exhibits symmetrical deformations. The maximum movement is 1 µm along the positive and negative y-axis in the curved region of the optical path. Additionally, a relatively small movement is observed along the positive and negative x-axis, with almost zero displacement along the z-axis. At the center of the optical path, which is also the center of the device, the motion along all three axes is nearly zero. This behavior was anticipated due to the configuration and location of the upper and lower comb drive actuators.

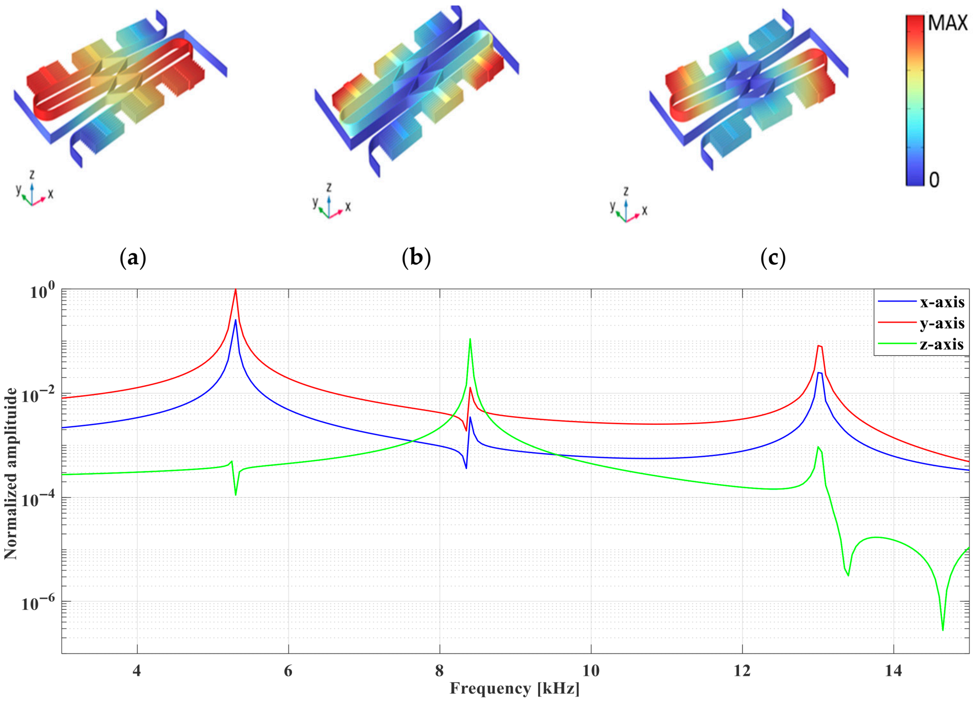

(**a**) (**b**) (**c**)

(**d**)

Figure 9. (**a**) First, (**b**) second, and (**c**) third resonant modes of the electrostatic MEMS optical phase shifter and its frequency spectra along the x-, y-, and z-axis.

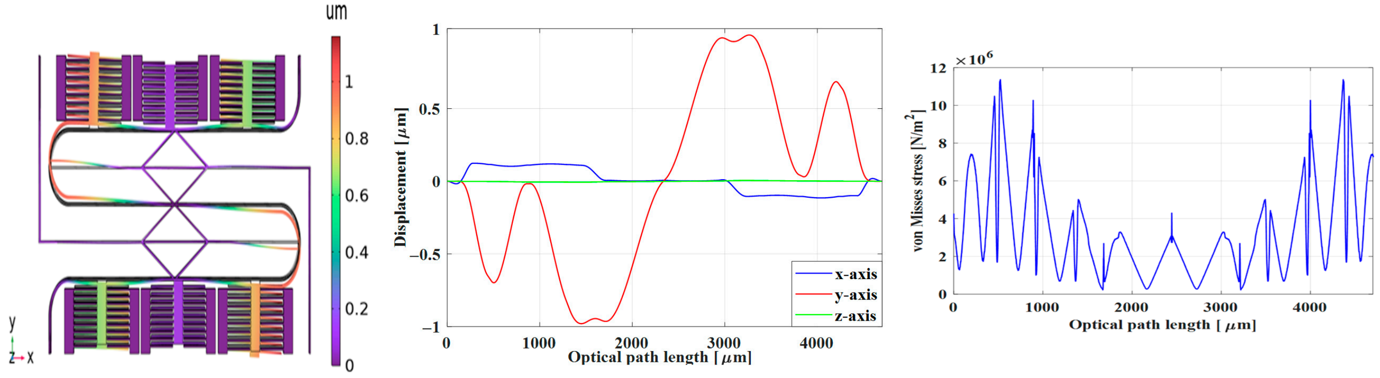

(**a**) (**b**) (**c**)

Figure 10. (**a**) Graphical representation of the deformation of the electrostatic optical MEMS phase shifter, (**b**) deformation profile, and (**c**) stress distribution of the optical path along its length.

Figure 10c illustrates the stress distribution experienced by the optical waveguide along its length. The stress distribution is symmetrical, similar to the deformation profile, with the pattern repeating after the center of the optical path at 2350 µm, showing mirrored repetition. It is noteworthy that the entire optical path is stressed, but areas in direct contact with the electrostatic actuators and near the anchors experience higher stresses.

To demonstrate the capability of controlling the stress amplitude in the optical waveguide through voltage activation of the electrostatic actuators, the average stress distribution along the optical path was computed with DC excitation voltages varying between 0 and 120 V. The results, shown in Figure 11a, indicate that the stress in the optical waveguide increases with the amplitude of the applied voltage, demonstrating a direct relationship between the applied voltage and induced stress. Figure 11b presents Δn_{eff} as a function of the voltage applied to the electrostatic actuators for a propagating wavelength of 1550 nm. The change in n_{eff} increases quadratically with the applied voltage. However, it is important to note that the applied voltage (and consequently the applied stress) must exceed a certain threshold to produce noticeable changes in n_{eff}. For example, an applied voltage below 30 V has minimal impact on n_{eff}.

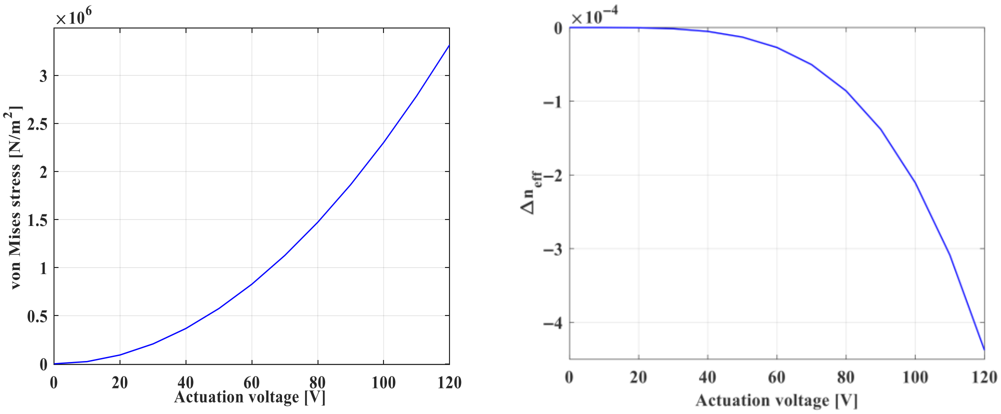

(**a**) (**b**)

Figure 11. (**a**) Average stress distribution in the optical waveguide, and (**b**) changes in the refractive index for different voltages.

One of the main advantages of SiN-based optical waveguides is their ability to operate across a wide wavelength range. To demonstrate the versatility of the proposed MEMS electrostatic optical phase shifter, its compatibility with the broadband properties of SiN was investigated. The absolute Δn_{eff} for the wavelength range from 1520 nm to 1620 nm was calculated and analyzed at a constant DC voltage of 120 V. As shown in Figure 12, the change in n_{eff} for the shortest wavelength (i.e., 1520 nm) is 4.43×10^{-4}. Δn_{eff} decreases slightly by 5% when the wavelength increases to 1620 nm, reaching 4.22×10^{-4}. According to (2) and the optical path length of the electrostatic MEMS phase shifter (i.e., 4.7 mm), the maximum phase shift at 1520 nm can be estimated to be 1.37 π, while the phase shift at 1620 nm is 1.22 π. The modulation frequency of the proposed electrostatic MEMS phase shifter is approximately 5.28 kHz, corresponding to its first mechanical resonance mode.

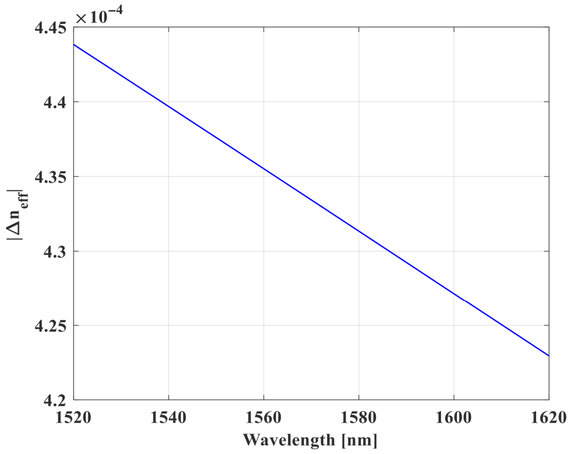

Figure 12. Absolute value of the effective index change, Δn_{eff} as a function of wavelength when the electrostatic actuators are activated with a 120 V DC voltage.

To this end, the proposed electrostatic MEMS optical phase shifter has demonstrated the ability to effectively and efficiently change the n_{eff} value by applying a voltage to its actuators. To further illustrate the phase-changing capability of the proposed approach, the optical phase shifter was implemented in one arm of an MZI. The simulation was conducted using a COMSOL Multiphysics 2D model (https://www.comsol.com/ accessed on 17 August 2025), incorporating *Boundary Mode Analysis*, *Stationary*, and *Frequency Domain* studies. Figure 13 shows the MZI output signals as a function of the actuating voltage on the electrostatic actuators. The performance of the phase shifter was evaluated for actuation voltages of 0 V, 80 V, and 120 V. The results indicate that a phase shift of almost π can be achieved when the electrostatic MEMS optical phase shifter is activated by a voltage of 80 V. Therefore, the half-wave voltage-length product ($V_\pi L$) of the proposed electrostatic MEMS optical phase shifter is 37.6 V·cm. The phase modulation can reach a maximum of 1.4 π when the actuators are activated by a DC voltage of 120 V. The required operating voltage can be delivered using CMOS-compatible DC–DC up-level converters or charge pumps [30]. It can further be observed that the proposed MEMS phase shifter does not compromise the broadband nature of the SiN waveguide, as the optical response remains constant across the entire wavelength range from 1548 nm to 1560 nm.

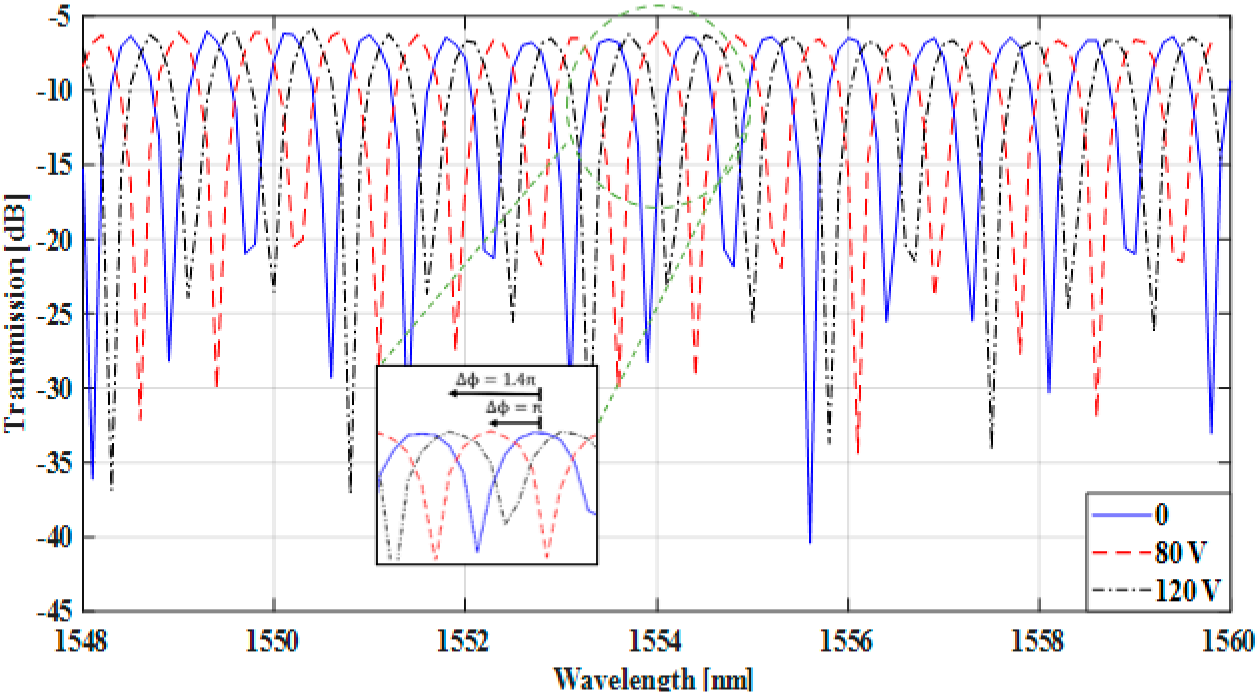

Figure 13. MZI output signals as a function of the actuating voltages of the electrostatic actuators.

The performance of the optical phase shifter proposed in this study was compared with state-of-the-art optical phase shifters, and the results are presented in Table 2. Thermo-optic phase shifters provide a compact modulation system; however, they require power on the order of milliwatts, making them impractical for low-power systems. Electro-optic phase shifters, while not power hungry, require a large optical path to achieve a sufficient phase shift, resulting in a footprint of several centimeters. Optical phase shifters based on physical movement consume almost no power and occupy a relatively small space, but their fabrication remains challenging.

Recent studies in [31,32] have demonstrated the implementation of phase shifters based on photo-elastic effects using piezoelectric materials to induce stress. However, the use of piezoelectric material increases the complexity of the fabrication process. Additionally, the study in [32] shows that an electrode size of 1 cm is needed to achieve a sufficient phase shift. In contrast, the electrostatic MEMS optical phase shifter proposed in this work is unique in that it does not require piezoelectric material to induce mechanical stress. The physical dimensions listed in Table 2 refer solely to the proposed MEMS phase shifter and do not include the entire MZI. While the proposed design can achieve near-zero power consumption, a highly desirable feature for reconfigurable MEMS-based silicon photonic integrated circuits, further improvements in actuation voltage and device footprint may be required to enhance its competitiveness relative to conventional phase shifter techniques. A glance at the listed $V\pi \cdot L$ values suggests that further reduction in the actuation voltage of the proposed phase shifter could significantly enhance its overall efficiency, making it comparable to thermo-optic and electro-optic techniques. One applicable approach to achieving this is by minimizing the air gap between the electrostatic actuator fingers, which would directly contribute to lowering the required actuation voltage.

Table 2. Performance comparison between the proposed electrostatic MEMS optical phase shifter and the state of the art.

Parameters **Reference**	**Type**	**Core**	**Cladding**	**Footprint (µm × µm)**	**V_π (V)**	**V_π L (V.cm)**	**P_π (mW)**
Sibton (2022) [33]	Thermo-optic	Si	SiO_2	320 × 1	36.4	1.16	24.9
C. Harris (2014) [34]	Thermo-optic	Si	SiO_2	61.6 × 20	4.36	0.26	24.77
Zhou (2021) [35]	Electro-optic	Si	-	2000 *	8	1.6	-
Wang (2018) [36]	Electro-optic	$LiNbO_3$	SiO_2	5000 *	4.4	-	-
Zhu (2016) [37]	Electro-optic	AlN	SiO_2	14,000 × 4000	171	240	-
Suzuki (2006) [38]	Electro-optic	$LiNbO_3$	-	170,000 × 36,000	9.5	11.97	-
Sattari (2019) [39]	Physical movement	Si	Air	60 × 40	19	0.32	~0
Grottke (2022) [40]	Physical movement	SiN	Air	360 × 240	4.5	-	~0
Stanfield (2019) [31]	Photo-elastic	SiN	SiO_2	960 × 1176 $^{+}$	40	-	-
Everhardt (2022) [32]	Photo-elastic	SiN	SiO_2	10,000 *	16	16	0.001
This work	Photo-elastic	SiN	SiO_2	1400 × 850	80	37.6	~0

* Width is not reported. + Estimated.

6. Conclusions

This study proposes a design for a configurable optical phase shifter based on photo-elastic effects. The phase shifter features a serpentine suspended SiN optical waveguide with a series of electrostatic MEMS actuators positioned nearby. When these electrostatic actuators are excited with a DC voltage, the optical waveguide is subjected to mechanical stress. The design is fully compatible with a previously demonstrated custom silicon photonics MEMS fabrication process and requires a footprint of 1400 µm × 850 µm. The performance of the electrostatic optical MEMS phase shifter was comprehensively investigated through numerical simulations. Implementing the phase shifter into one arm of an unbalanced MZI demonstrated that a phase shift of 1.4 π can be achieved at a DC voltage of 120 V with almost zero power consumption. Exciting the actuators with a DC voltage of 80 V results in a phase shift of π, corresponding to a half-wave voltage-length product ($V_\pi L$) of 37.6 V·cm. A comparative analysis with state-of-the-art optical phase shifters highlights the advantages of the proposed design in terms of power efficiency, compactness, and simplified fabrication, making it an efficient component for reconfigurable MEMS-based silicon photonic integrated circuits.

Author Contributions: Conceptualization, S.N., M.M. and F.N.; methodology, S.N.; software, S.N.; validation, S.N., M.M. and F.N.; formal analysis, S.N.; resources, M.M. and F.N.; writing—original draft preparation, S.N.; writing—review and editing, M.M. and F.N.; supervision, M.M. and F.N.; project administration, M.M. and F.N.; funding acquisition, M.M. and F.N. All authors have read and agreed to the published version of the manuscript.

Funding: This research was funded by Natural Sciences and Engineering Research Council of Canada (NSERC), PRIMA Québec, and AEPONYX Inc.

Data Availability Statement: The original contributions presented in this study are included in the article. Further inquiries can be directed to the corresponding author.

Conflicts of Interest: S. Nabavi, M. Ménard, and F. Nabki received grants from the Natural Sciences and Engineering Research Council of Canada (NSERC), PRIMA Québec (a funding agency supported by the government of the province of Québec, Canada) and AEPONYX Inc., a private company. AEPONYX participated in the design of the study and decision to publish the results. However, AEPONYX did not participate in the collection, analysis, or interpretation of data, nor in the writing of the manuscript.

References

1. Batten, C.; Joshi, A.; Orcutt, J.; Khilo, A.; Moss, B.; Holzwarth, C.W.; Popovic, M.A.; Li, H.; Smith, H.I.; Hoyt, J.L.; et al. Building Many-Core Processor-to-DRAM Networks with Monolithic CMOS Silicon Photonics. *IEEE Micro* **2009**, *29*, 8–21. [CrossRef]
2. Reed, G.; Thomson, D.; Zhang, W.; Gardes, F.; Mastronardi, L.; Li, K.; Matsuo, S.; Kanazawa, S.; Vivien, L.; Lafforgue, C.; et al. Optical Modulators. In *Integrated Photonics for Data Communication Applications*; Elsevier: Amsterdam, The Netherlands, 2023; pp. 69–121.
3. Wang, H.; Liu, W.; Pan, Z.; Tao, Y.; Niu, J.; Tang, J.; Liu, J. Suppression of Backscattering-Induced Noise in a Resonator Optic Gyro by the Dual-Frequency Modulation Method. *Opt. Commun.* **2020**, *459*, 124766. [CrossRef]
4. Sun, X.; Feng, J.; Zhong, L.; Lu, H.; Han, W.; Zhang, F.; Akimoto, R.; Zeng, H. Silicon Nitride Based Polarization-Independent 4×4 Optical Matrix Switch. *Opt. Laser Technol.* **2019**, *119*, 105641. [CrossRef]
5. Jacques, M.; Samani, A.; El-Fiky, E.; Patel, D.; Xing, Z.; Plant, D. V Optimization of Thermo-Optic Phase-Shifter Design and Mitigation of Thermal Crosstalk on the SOI Platform. *Opt. Express* **2019**, *27*, 10456–10471. [CrossRef]
6. Chmielak, B.; Waldow, M.; Matheisen, C.; Ripperda, C.; Bolten, J.; Wahlbrink, T.; Nagel, M.; Merget, F.; Kurz, H. Pockels Effect Based Fully Integrated, Strained Silicon Electro-Optic Modulator. *Opt. Express* **2011**, *19*, 17212–17219. [CrossRef] [PubMed]
7. Janner, D.; Tulli, D.; Garcia-Granda, M.; Belmonte, M.; Pruneri, V. Micro-Structured Integrated Electro-Optic LiNbO3 Modulators. *Laser Photon. Rev.* **2009**, *3*, 301–313. [CrossRef]
8. Leuthold, J.; Koos, C.; Freude, W.; Alloatti, L.; Palmer, R.; Korn, D.; Pfeifle, J.; Lauermann, M.; Dinu, R.; Wehrli, S.; et al. Silicon-Organic Hybrid Electro-Optical Devices. *IEEE J. Sel. Top. Quantum Electron.* **2013**, *19*, 114–126. [CrossRef]
9. Gräupner, P.; Pommier, J.C.; Cachard, A.; Coutaz, J.L. Electro-Optical Effect in Aluminum Nitride Waveguides. *J. Appl. Phys.* **1992**, *71*, 4136–4139. [CrossRef]
10. Xiong, C.; Pernice, W.H.P.; Tang, H.X. Low-Loss, Silicon Integrated, Aluminum Nitride Photonic Circuits and Their Use for Electro-Optic Signal Processing. *Nano Lett.* **2012**, *12*, 3562–3568. [CrossRef]
11. Edinger, P.; Takabayashi, A.Y.; Errando-Herranz, C.; Khan, U.; Sattari, H.; Verheyen, P.; Bogaerts, W.; Quack, N.; Gylfason, K.B. Silicon Photonic Microelectromechanical Phase Shifters for Scalable Programmable Photonics. *Opt. Lett.* **2021**, *46*, 5671–5674. [CrossRef] [PubMed]
12. Shea, H.R.; Gasparyan, A.; Chan, H.B.; Arney, S.; Frahm, R.E.; López, D.; Jin, S.; McConnell, R.P. Effects of Electrical Leakage Currents on MEMS Reliability and Performance. *IEEE Trans. Device Mater. Reliab.* **2004**, *4*, 198–207. [CrossRef]
13. Nabavi, S.; Zhang, L. Curve-Shaped Anchor for Durability and Efficiency Improvement of Piezoelectric MEMS Energy Harvesters. In Proceedings of the 2018 IEEE SENSORS, New Delhi, India, 28–30 October 2018; pp. 1–4.
14. Sebbag, Y.; Goykhman, I.; Desiatov, B.; Nachmias, T.; Yoshaei, O.; Kabla, M.; Meltzer, S.E.; Levy, U. Bistability in Silicon Microring Resonator Based on Strain Induced by a Piezoelectric Lead Zirconate Titanate Thin Film. *Appl. Phys. Lett.* **2012**, *100*, 141107. [CrossRef]
15. Wang, J.; Liu, K.; Harrington, M.W.; Rudy, R.Q.; Blumenthal, D.J. Silicon Nitride Stress-Optic Microresonator Modulator for Optical Control Applications. *Opt. Express* **2022**, *30*, 31816–31827. [CrossRef]
16. Roeloffzen, C.G.H.; Hoekman, M.; Klein, E.J.; Wevers, L.S.; Timens, R.B.; Marchenko, D.; Geskus, D.; Dekker, R.; Alippi, A.; Grootjans, R.; et al. Low-Loss Si3N4 TriPleX Optical Waveguides: Technology and Applications Overview. *IEEE J. Sel. Top. quantum Electron.* **2018**, *24*, 1–21. [CrossRef]
17. Zhang, L.; Li, Y.; Hou, Y.; Wang, Y.; Tao, M.; Chen, B.; Na, Q.; Li, Y.; Zhi, Z.; Liu, X.; et al. Investigation and Demonstration of a High-Power Handling and Large-Range Steering Optical Phased Array Chip. *Opt. Express* **2021**, *29*, 29755–29765. [CrossRef] [PubMed]
18. Romero-Garcia, S.; Merget, F.; Zhong, F.; Finkelstein, H.; Witzens, J. Silicon Nitride CMOS-Compatible Platform for Integrated Photonics Applications at Visible Wavelengths. *Opt. Express* **2013**, *21*, 14036–14046. [CrossRef] [PubMed]

19. Orfanos, V.A.; Kaminaris, S.D.; Papageorgas, P.; Piromalis, D.; Kandris, D. A Comprehensive Review of IoT Networking Technologies for Smart Home Automation Applications. *J. Sens. Actuator Netw.* **2023**, *12*, 30. [CrossRef]
20. Sharma, A.; Chaudhary, S.; Malhotra, J.; Khichar, S.; Wuttisittikulkij, L. Photonic Sensor for Multiple Targets Detection under Adverse Weather Conditions in Autonomous Vehicles. *J. Sens. Actuator Netw.* **2022**, *11*, 60. [CrossRef]
21. Jenkins, F.A.; White, H.E. Fundamentals of Optics. *Indian J. Phys.* **1957**, *25*, 265–266. [CrossRef]
22. Lockwood, D.J.; Pavesi, L. *Silicon Photonics*; Springer: Berlin/Heidelberg, Germany, 2004.
23. Ye, W.; Mukherjee, S.; MacDonald, N.C. Optimal Shape Design of an Electrostatic Comb Drive in Microelectromechanical Systems. *J. Microelectromechanical Syst.* **1998**, *7*, 16–26. [CrossRef]
24. Sharma, S.; Kohli, N.; Brière, J.; Nabki, F.; Ménard, M. Integrated 1*3 MEMS Silicon Nitride Photonics Switch. *Opt. Express* **2022**, *30*, 22200–22220. [CrossRef]
25. Heidari, N.; Pita Ruiz, J.L.; Nabavi, S.; Ménard, M.; Nabki, F. Reconfigurable Electrostatically Actuated 1*5 Rotary MOEMS Switch. *Opt. Express* **2025**, *33*, 10726–10740. [CrossRef] [PubMed]
26. Nabavi, S.K.; Ménard, M.; Nabki, F. An Electrostatic Micropositioner with 3 Degrees-of-Freedom. In Proceedings of the 2023 IEEE SENSORS, Vienna, Austria, 29 October–1 November 2023; pp. 1–4.
27. Rabih, A.A.S.; Sharma, S.; Pita, J.; Ménard, M.; Nabki, F. Two-Axis MEMS Positioner for Waveguide Alignment in Silicon Nitride Photonic Integrated Circuits. *Opt. Express* **2023**, *31*, 30797–30814. [CrossRef]
28. Sharma, S.; Kohli, N.; Ménard, M.; Nabki, F. An Integrated 1 X 5 MEMS Silicon Nitride Photonics Switch. *J. Light. Technol.* **2024**, *42*, 4585–4597. [CrossRef]
29. AEPONYX Inc. Available online: https://www.aeponyx.com/ (accessed on 19 February 2024).
30. Ismail, Y. *High-Voltage Generation and Drive in Low-Voltage CMOS Technology*; University of California: Los Angeles, CA, USA, 2015.
31. Stanfield, P.R.; Leenheer, A.J.; Michael, C.P.; Sims, R.; Eichenfield, M. CMOS-Compatible, Piezo-Optomechanically Tunable Photonics for Visible Wavelengths and Cryogenic Temperatures. *Opt. Express* **2019**, *27*, 28588–28605. [CrossRef]
32. Everhardt, A.S.; Tran, T.L.A.; Mitsolidou, C.; Horner, T.R.; Grootjans, R.; Oldenbeuving, R.; Heuvink, R.; Geuzebroek, D.; Leinse, A.; Roeloffzen, C.; et al. Ultra-Low Power Stress-Based Phase Actuation in TriPleX Photonic Circuits. In Proceedings of the Integrated Optics: Devices Materials, and Technologies XXVI, San Francisco, CA, USA, 22–27 January 2022; Volume 12004, pp. 15–21.
33. Sitbon, E.; Ostrovsky, R.; Malka, D. Optimizations of Thermo-Optic Phase Shifter Heaters Using Doped Silicon Heaters in Rib Waveguide Structure. *Photonics Nanostructures-Fundam. Appl.* **2022**, *51*, 101052. [CrossRef]
34. Harris, N.C.; Ma, Y.; Mower, J.; Baehr-Jones, T.; Englund, D.; Hochberg, M.; Galland, C. Efficient, Compact and Low Loss Thermo-Optic Phase Shifter in Silicon. *Opt. Express* **2014**, *22*, 10487–10493. [CrossRef]
35. Zhou, J.; Wang, J.; Zhu, L.; Zhang, Q. Silicon Photonics for 100Gbaud. *J. Light. Technol.* **2021**, *39*, 857–867. [CrossRef]
36. Wang, C.; Zhang, M.; Chen, X.; Bertrand, M.; Shams-Ansari, A.; Chandrasekhar, S.; Winzer, P.; Lončar, M. Integrated Lithium Niobate Electro-Optic Modulators Operating at CMOS-Compatible Voltages. *Nature* **2018**, *562*, 101–104. [CrossRef]
37. Zhu, S.; Lo, G.-Q. Aluminum Nitride Electro-Optic Phase Shifter for Backend Integration on Silicon. *Opt. Express* **2016**, *24*, 12501–12506. [CrossRef]
38. Suzuki, K.; Yamada, T.; Ishii, M.; Shibata, T.; Mino, S. High-Speed Optical 1 × 4 Switch Based on Generalized Mach–Zehnder Interferometer With Hybrid Configuration of Silica-Based PLC and Lithium Niobate Phase-Shifter Array. *IEEE Photonics Technol. Lett.* **2007**, *19*, 674–676. [CrossRef]
39. Sattari, H.; Graziosi, T.; Kiss, M.; Seok, T.J.; Han, S.; Wu, M.C.; Quack, N. Silicon Photonic MEMS Phase-Shifter. *Opt. Express* **2019**, *27*, 18959–18969. [CrossRef] [PubMed]
40. Grottke, T.; Hartmann, W.; Schuck, C.; Pernice, W.H.P. Optoelectromechanical Phase Shifter with Low Insertion Loss and a 13π Tuning Range. *Opt. Express* **2021**, *29*, 5525–5537. [CrossRef] [PubMed]